Additively Manufactured Robust Microfluidics via Silver Clay Extrusion

Emmanuel Segura-Cárdenas and Luis Fernando Velásquez-García, *Senior Member, IEEE*

***Abstract*— We report novel, low-cost, high-temperature compatible, high-pressure compatible, and chemically resistant additively manufactured microfluidics. The devices were monolithically fabricated by extruding silver clay with a fused filament fabrication 3D printer frame fitted with a syringe extruder, followed by annealing at 885 °C in air. Analysis of the printable feedstock shows that the green material is an alloy composed of silver and copper microparticles blended with an organic binder matrix, while analysis of printed and annealed samples shows that the material is completely free of binder and compatible with at least 800 °C operation. Characterization of the thermal, electrical, and mechanical properties of printed and annealed structures yields values close to those of bulk sterling silver, except for a significantly smaller Young's modulus. Metrology of test structures evidences linearity between printed dimensions and computer-aided design values. Layers as thin as 150 μm and working, watertight closed channels as narrow as 200 μm were consistently resolved. A proof-of-concept microfluidic that catalytically decomposes hydrogen peroxide was designed, fabricated, and characterized; the experimental performance of the catalytic microreactor is in agreement with reduced-order modeling. [2019-0267]**

***Index Terms*— 3D printing of MEMS, catalyst, hydrogen peroxide, microfluidics, microreactor, silver clay.**

I. Introduction

MICROFLUIDICS are devices that process or manipulate small volumes of fluid (typically nanoliters to microliters) using channels with sub-millimeter and smaller hydraulic diameter, i.e. microchannels [1]. Most microfluidics use a network of closed microchannels (i.e. an interconnected arrangement of long and narrow internal voids connected to one or more external fluidic ports) to efficiently accomplish tasks such as species mixing, heat transfer, particle sorting, and other surface-to-volume-ratio-enhanced processes [2].

The great majority of microfluidics are made of silicone rubbers, e.g. polydimethylsiloxane (PDMS), which allow visual monitoring of the flow dynamics from the outside [3]–[5]; however, these materials don't withstand high temperatures or high pressures, neither are resilient to strong acids, alkalis and organic solvents—liquids often used for chemical synthesis and decomposition. More robust microfluidics can be made via silicon and glass micromachining [6], [7] or ceramic lamination [8]; however, these materials are fragile and their associated manufacturing methods involve high cost, long production time, no device customization, and elaborate design iteration. Metals are a good choice for manufacturing rugged microfluidics, as they are in general strong, ductile, shock resistant, high-temperature compatible, high-pressure compatible, and chemically resistant; moreover, transition metals have catalytic properties that can be used in the chemical processing conducted by the microfluidic device; nonetheless, microfabrication technology for metals focuses on thin films and wafer bonding [3]. In addition, fabrication approaches such as electric discharge micromachining [9] and micro milling [10] have been explored to implement metal microfluidics, but these manufacturing processes are very expensive, very slow, and require specialized tooling.

Additive manufacturing, i.e. the maskless, layered creation of solid structures following a computer-aided design (CAD) model, has been recently explored as a toolbox to implement microsystems, particularly microfluidics [11]–[15]. However, most 3D-printed microfluidics are made of polymers that are not compatible with the aforementioned harsh conditions and fluids. Conventional metal 3D printing methods include lost-wax micromolding [16], inkjet binder [17] and direct metal laser sintering [18]; unfortunately, these processes are not ideal for producing monolithic, closed-channel microfluidics because they either require internal dummy structures to define internal voids, or create parts with internal voids filled with unprinted feedstock—both of which are difficult to remove to have functional devices.

Fused filament fabrication (FFF) is a 3D printing technique that creates solid objects via extrusion of thermoplastics using one or more hot nozzles that raster, layer by layer, a volume defined by a CAD file [19]. There are quite a few examples of FFF-printed microfluidics [20]; although a few of these reported devices are made in chemically resistant polymers, e.g. polypropylene (PP), these materials can only operate within a moderate range of pressures and temperatures, and have no catalytic properties.

Metal clay extrusion is a novel 3D printing technique compatible with microfluidics manufacturing that creates objects in much the same way as traditional plastic extruding, although without involving heat in the extrusion process. Metal clays are slurries of metal microparticles mixed with a water-soluble

Manuscript received December 17, 2019; revised March 13, 2020; accepted March 18, 2020. Date of publication April 6, 2020; date of current version June 2, 2020. This work was supported in part by the Monterrey Tec-MIT Nanotechnology Program. Subject Editor K. Cheung. *(Corresponding author: Luis Fernando Velásquez-García.)*

Emmanuel Segura-Cárdenas was with the Microsystems Technology Laboratories, Massachusetts Institute of Technology, Cambridge, MA 02139 USA. He is now with the Departamento de Ingeniería Mecánica y Materiales Avanzados, Tecnologico de Monterrey, Escuela de Ingenieria y Ciencias, Monterrey 64849, Mexico (e-mail: esca@tec.mx).

Luis Fernando Velásquez-García is with the Microsystems Technology Laboratories, Massachusetts Institute of Technology, Cambridge, MA 02139 USA (e-mail: velasquez@alum.mit.edu).

Color versions of one or more of the figures in this article are available online at http://ieeexplore.ieee.org.

Digital Object Identifier 10.1109/JMEMS.2020.2982559

organic binder that were invented in the 1990s to allow making complex jewelry without requiring extensive training [21]. The metal clay is a thick paste that can be extruded, dried, and annealed at high temperature to produce solid metal objects; annealing of the green (i.e. as-printed) objects typically causes them to shrink up to 15%. Metal clay extrusion offers key advantages over the other 3D printing methods for metal including (i) inexpensive printing hardware, (ii) low per-device cost, (iii) room-temperature printing of the green objects, (iv) no emission of particles or fumes during printing, and (v) feasibility to create watertight structures with internal voids via bridging (i.e. extrusion of feedstock across a gap, without structural support within the gap [22]).

In this study, we explore metal clay extrusion as a 3D printing technology to implement monolithic, low-cost, and rugged microfluidics using silver clay as printable feedstock. Silver clay was chosen as printable material because is compatible with a wide range of microfluidics, from heat exchangers to microreactors, given its high thermal and electrical conductivities, chemical resistance, and catalytic properties. Other printable feedstock were also considered, but were discarded as they present significant disadvantages compared to silver:

- bronze is cheaper than silver, but bronze clay needs to be annealed in an oxygen-free environment, which is typically accomplished using a vacuum furnace or particle-generating carbon feedstock next to the printed part;
- gold has excellent chemical, electrical, and heat transfer properties, as well as catalytic properties, but is an 85-fold more expensive than silver;
- copper has excellent electrical and heat transfer properties, and is cheaper than silver, but copper is more reactive than silver, e.g. it can degrade more easily when used as a catalyst.

Section II describes the fabrication process using a modified FFF 3D printer, while Section III reports the metrology characterization of test structures, and Section IV details the material characterization of green and annealed structures. Section V summarizes the electrical, thermal, and mechanical characterization of the annealed feedstock, while Section VI reports the design, fabrication, and characterization of a proof-of-concept microreactor that catalytically decomposes hydrogen peroxide as an example of a microfluidic that can be made via silver clay extrusion. Finally, Section VII summarizes the work.

II. Fabrication

Test structures and devices were additively manufactured with a PC-controlled FFF 3D printer frame fitted with a high-torque gear reduction that can deliver over 300 pounds of force to the plunger of a syringe filled with metal clay [23]. The printer extrudes metal clay at room temperature through a 400 μm-diameter nozzle; the extruded material is collected on a build plate, i.e. a sheet of bonded magnet that attaches to the top of the printer platform. During printing, the pressure acting on the clay reservoir of the syringe can be rapidly modulated with the gearbox reduction, allowing for precise control of the clay flow —a potentiometer controlling the motor that actuates the syringe allows for fine tuning of the clay reservoir pressure, ensuring continuous flow at a given nozzle rastering speed.

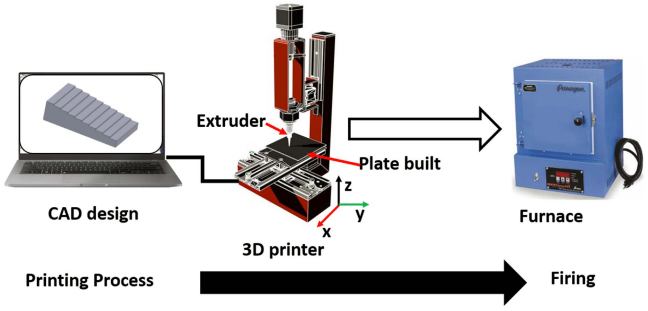

Fig. 1. Schematic of 3D printing process to create metal clay-extruded objects.

To print a structure (Fig. 1), a CAD model is created in STL format (SolidWorks 2015, Dassault Systèmes, Waltham, MA, USA) and exported to a slicer software (Simplify3D, Cincinnati, OH, USA), which is a script that discretizes the CAD model into a set of horizontal cuts, i.e. slices, and creates a G-code file with the traveling path of the nozzle to raster each slice with associated conditions (e.g. rastering speed, nozzle flow rate). The G-code file is then transferred to the 3D printer, which, following the G-code, rasters the build plate while spreading silver clay (EZ960, Cool Tools, Jefferson, WI, USA). After printing, the build plate is detached from the printer platform and stored in a desiccator for 12 hours at 20% humidity to allow the printed object to dry; the green object is then carefully removed from the build plate and transferred to an air kiln to be annealed for 4 h @ 885 °C, burning out all the organic binder of the clay. No post-treatment of the printed objects, e.g. polishing, was carried out.

III. Metrology Characterization

Green and annealed test structures were measured with a confocal microscope Keyence CX-X200 Series (Keyence, Osaka, Japan) to characterize the in-plane and out-of-plane resolution and repeatability of printed positive (solid) features, as well as the in-plane resolution and repeatability of negative (void) features. The data show linearity between the dimensions of green structures and corresponding CAD values, and between the dimensions of annealed structures and corresponding CAD values. Positive in-plane, positive out-of-plane, and negative in-plane dimensions of green structures are about 92% CAD values; positive in-plane, positive out-of-plane, and negative in-plane dimensions of annealed structures are about 81%, within about 6%, and about 80% CAD values, respectively. However, the shrinkage values significantly vary depending on the slicing height. Watertight, closed microchannels as narrow as 200 μm were demonstrated.

To first order, based on the scaling factors obtained in these experiments, one can compensate the shrinkage from printing and annealing to create a final part with dimensions very close to those intended. However, in our experience it is challenging to completely eliminate the mismatch between actual dimensions and intended dimensions. In our opinion, the reasons for this result include:

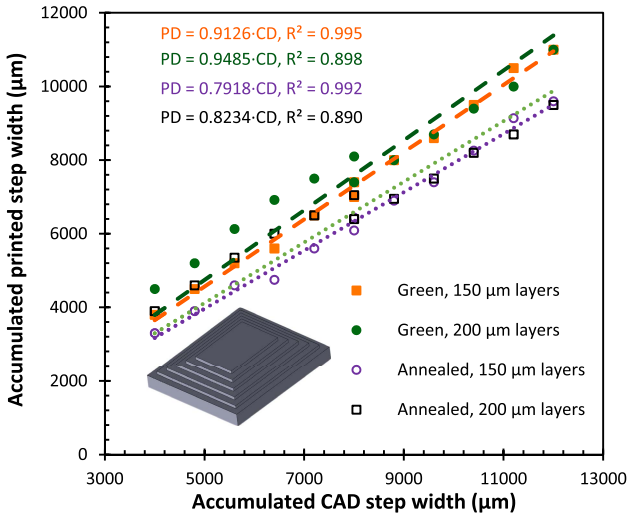

Fig. 2. Accumulated printed step width vs. CAD dimension, measured before and after annealing, of step pyramid test structures. In the least-squares fittings, PD = printed dimension, CD = CAD dimension. Solid markers denote data from as-printed objects, while hollow markers denote data from annealed objects. Least-squares fittings of green data are dashed lines, while least-squares fittings of annealed data are dotted lines.

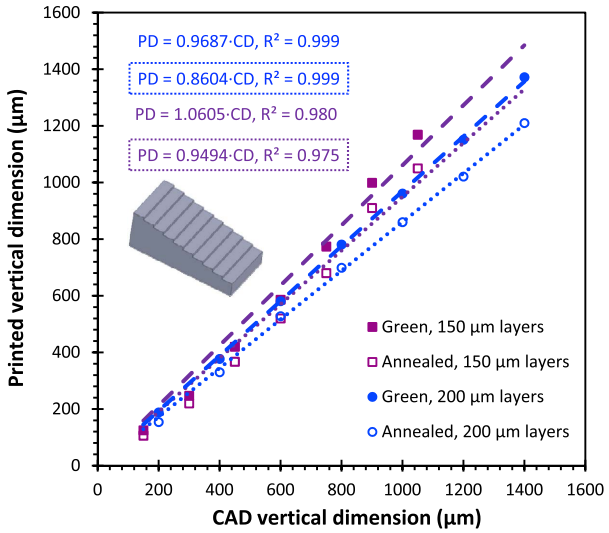

Fig. 3. Out-of-plane printed dimension vs. corresponding CAD dimension, measured before and after annealing, of stairs-like test structures. In the least-squares fittings, PD = printed dimension, CD = CAD dimension. Solid markers denote data from green structures, while hollow markers denote data from annealed structures. Least-squares fittings of green data are dashed lines, while least squares fittings of annealed data are dotted lines.

- The pressure acting on the syringe clay reservoir needs to be finely tuned every time a new printing job is run to make sure the material flows satisfactorily. The tuning involves finely varying the force exerted by the piston to make sure the material flows uniformly at a given nozzle rastering speed.
- Clay extrusion is a printing method that does not involve XY pixels; pixels in combination with the layer height discretize into voxels the volume of the printed part, which makes the printing process more dimensionally robust.
- Clay extrusion involves high temperature annealing and feedstock made out of particles with size spread; issues such as temperature uniformity in the furnace used for annealing and local particle size variation influence the final dimensions of the part.

A. Positive In-Plane Feature Characterization

Step pyramids were printed using 150 μm-thick and 200 μm-thick layers and measured in both X and Y directions to characterize the resolution and repeatability of positive in-plane features; the data are shown in Fig. 2. Each pyramid had six steps on top of a 1 mm-thick plate monolithically printed with the steps. The structures spanned a combined range of CAD step width between 4000 μm and 12000 μm; 15 structures were printed and measured at random in 4 points within each step (i.e. each data point in Fig. 2 is the average of 60 measurements). The steps were centered around the vertical axis of the pyramid, and the separation between the edges of adjacent steps was set at 400 μm in the CAD files. Metrology of the test structures evidences linearity between the CAD and printed in-plane features for both green and annealed structures. On average, the dimensions of the green structures are 93% the CAD values, while the dimensions of the annealed structures are 81% the CAD values (i.e. the in-plane features of the annealed structures shrink about 13% from the dimensions of the green structures). No significant difference between measurements in the X and Y directions was found, although the structures made with the coarser slicing (i.e. 200 μm layer height) have associated less size variation and closer correspondence to the CAD files.

B. Positive Out-of-Plane Feature Characterization

Stair-like structures were printed and measured to characterize the resolution and repeatability of positive out-of-plane features; the data are shown in Fig. 3. Each structure had a total of 9 steps on top of a 1 mm-thick base plate that was monolithically printed with the steps. The height of the steps is the nominal slice height, which was set at 150 μm or 200 μm; 15 structures were printed and measured at random in four points within each step (i.e. each data point in Fig. 3 is the average of 60 measurements), spanning 150 μm to 1400 μm in the CAD files. In all cases, we found that the height of the base of the printed stair structure was equal to 0.98 mm instead of 1 mm, probably reflecting the out-of-plane offset typically present in the first layer printed by an FFF 3D printer [22]. The slice height of the green layers is significantly closer to the CAD values for the coarser slicing (197.3 μm $\pm$ 14.4 μm for 200 μm CAD slices, 174.0 μm $\pm$ 33.4 μm for 150 μm CAD slices); after annealing, the slice height shrinks about 9% from green values (176.0 μm $\pm$ 15.0 μm for 200 μm CAD slices, 157.3 μm $\pm$ 39.0 μm for 150 μm CAD slices). The least-squares fittings of the data show linearity between the out-of-plane dimensions of green and annealed structures compared to CAD values: features of green structures are about 92% the CAD values, while the dimensions of annealed structures are between 95% and 106% CAD values.

C. Negative In-Plane Feature Characterization

Comb structures were printed and measured to characterize the resolution and repeatability of negative in-plane features;

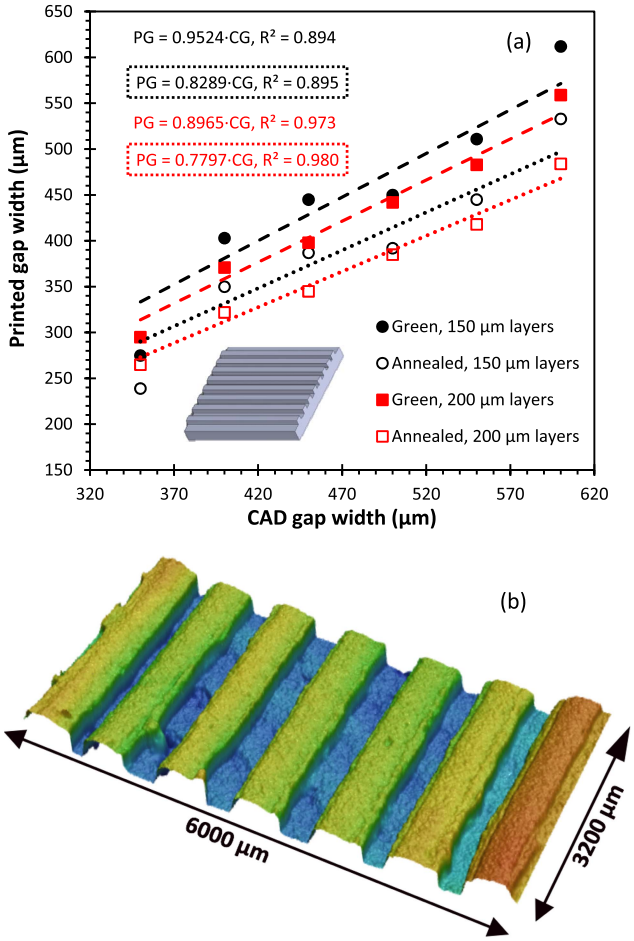

Fig. 4. (a) Printed gap width vs. CAD gap width; in the least-squares fittings, PG = printed gap width, CG = CAD gap width. (b) Confocal micrograph of a test structure printed in 150 μm-tall layers; the trenches between the fingers are 200 μm wide.

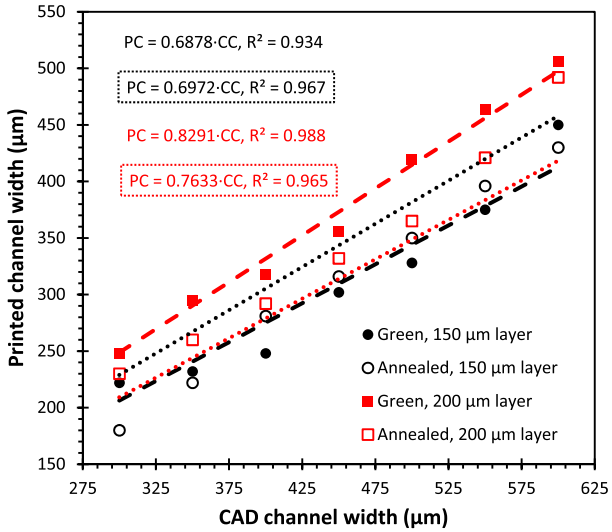

Fig. 5. Closed microchannel width vs. corresponding CAD dimension measured before and after annealing. In the least-squares fittings, PC = printed channel width, CC = CAD channel width. Solid markers denote data from green structures, while hollow markers denote data from annealed structures. Least-squares fittings of green data are dashed lines, while least squares fittings of annealed data are dotted lines.

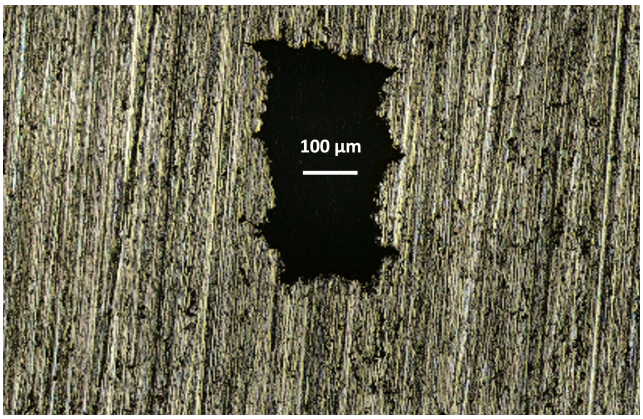

Fig. 6. Close-up micrograph of an annealed test structure with a watertight, 180 μm-wide by 400 μm-tall microchannel. The test structure was printed, dried, and carefully cut with a sharp edge before annealing; some smearing of the edge of the microchannel is visible due to the cutting process. The scalloping due to the extrusion of the feedstock during printing is also visible.

the combs had varying finger separation and were on top of a 1-mm thick plate that was monolithically printed with the comb structures. A set of 15 identical structures were printed using 150 μm or 200 μm layers; the fingers were 400 μm or 600 μm tall, 12 mm-long and 600 μm-wide, while the separation between adjacent fingers was varied between 350 μm and 600 μm in steps of 50 μm in the CAD files. For each test structure, the gap between the fingers was measured in 3 random points across the length of the fingers; the results of the metrology are shown in Fig. 4. The least-squares fittings of the data show linearity between the green and annealed negative features and the CAD values, where the green features are about 92% the CAD values, and the annealed features are about 80% the CAD values (i.e. the annealed void features shrink about 13% from green values). Uniform gaps as narrow as 200 μm were successfully created (Fig. 4b).

Based on the metrology results of the comb structures, printing of closed, 12 mm-long microchannel structures was carried out using 150 μm-thick and 200 μm-thick layers; the microchannels were created on top of a 1-mm thick plate. Preliminary experiments showed that channels with height equal to one layer collapse after annealing; consequently, in the CAD files the channels were between 300 μm and 600 μm tall (i.e. 2 to 4 slices), while the channel width was varied between 300 μm and 600 μm in steps of 50 μm. On average, channel width shrinks about 27% from CAD values (Fig. 5); the narrowest microchannel consistently printed is about 200 μm wide after annealing (Fig. 6). The minimum width of the channels definable by silver clay extrusion is on par or better than reported values from FFF-printed microfluidics made in a wide variety of polymers [20].

IV. Characterization of Printable Feedstock

Analysis of the printable feedstock included scanning electron microscopy (SEM), energy dispersive spectroscopy (EDS), thermogravimetric analysis (TGA), and X-ray diffraction (XRD) techniques. The data show that the green material is composed of silver and copper microparticles blended with an organic binder matrix, while analysis of annealed samples shows that the material is sterling silver completely free of binder. The data also demonstrate that the printable material

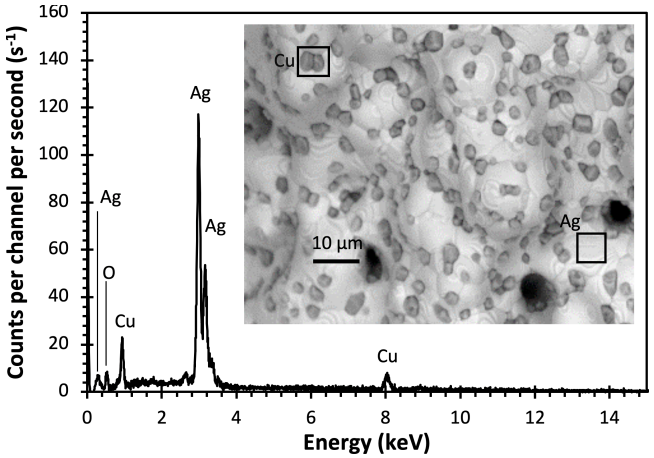

Fig. 7. Chemical (EDS) and microstructural (SEM inset) analysis of annealed silver clay.

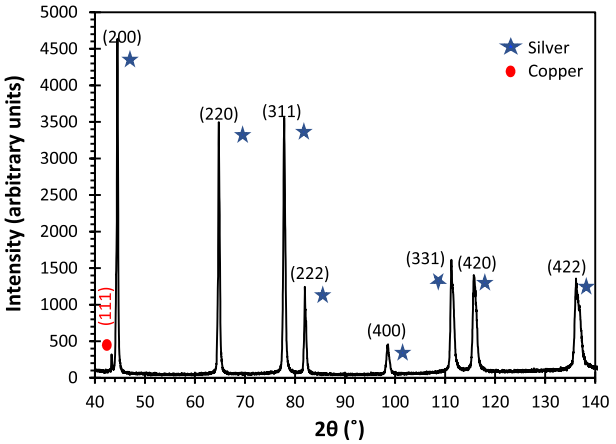

Fig. 8. XRD pattern of the annealed material. The data show that the material is sterling silver–an alloy majoritarily composed of silver with traces of copper.

has dibutyl phthalate as solvent and ethyl-cellulose as binder; in addition, the data demonstrate that the printed material is compatible with at least 800 °C operation.

A. EDS and SEM Characterization of Annealed Feedstock

The quantitative and qualitative composition of annealed samples of the printable feedstock were investigated using an EVO MA25 ZEISS SEM equipped with an EDS micro analytical system (ZEISS, Jena, Germany); the data are shown on Fig. 7. SEM micrographs (Fig. 7 inset) show that the annealed material is an alloy made of copper microparticles dispersed in a matrix of silver-rich compounds. EDS analysis demonstrates that the composition of the material is 9% copper phase, 82% silver phase, and 9% oxygen; the oxygen present is due to the formation of a thin oxide film on the surface of the sample.

B. XRD Characterization of Annealed Feedstock

The XRD pattern of the annealed material is presented in Fig. 8; the data were captured with a PanAnalytical X'Pert Pro PW1800 diffractometer Malvern (Panalytical B.V., Eindhoven, The Netherlands). Diffraction peaks at 38.2°, 44.3°, 64.4° and 77.5° are observed, which correspond to the silver phase with a face-centered cubic (FCC) crystalline structure;

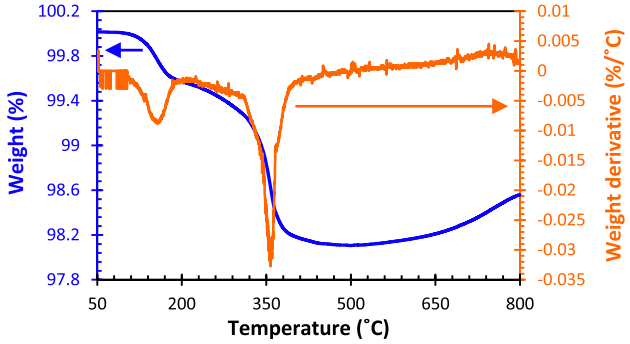

Fig. 9. TGA of as-purchased silver metal clay, i.e. sample weight percentage versus temperature, and derivative of weight percentage with respect to temperature versus temperature.

the data are in accordance with the standard diffraction pattern [24]. There is also a peak located at 43.3°, which corresponds to the copper phase with FCC structure, also in agreement to the standard [25]. The diffraction pattern is dominated by the silver phase, with a low amount of copper, because the material is sterling silver—an alloy majoritarily composed of silver with traces of copper.

C. TGA Characterization of Printable Feedstock

TGA analysis of the silver metal clay was carried out under air atmosphere and at a temperature between 100 °C and 800 °C with a heating rate of 10 °C/min (TA Instruments, New Castle, DE, USA). The decomposition of the clay occurs in two events, as shown in Fig. 9. First, a small weigh loss of 0.4% takes place around 156 °C, which is related to the degradation of dibutyl phthalate [26]—an organic solvent commonly used to promote plasticity in a clay formulation. The second weight loss event is significantly larger (a few percent) and occurs at 356 °C; this weight loss is attributed to the decomposition of ethyl-cellulose [27]—the binder of the formulation. There is a small weight increase for temperatures above 500 °C that is related to the presence of copper in low quantities in the clay, which creates a thin oxide film on the surface of the alloy. There is no peak associated to the degradation of the silver, demonstrating that the printable material is compatible with operation at temperatures as high as at least 800 °C.

V. Physical Properties of Annealed Feedstock

The electrical resistivity, thermal conductivity, Young's modulus, yield stress, and ultimate tensile stress of annealed feedstock were estimated from experiments and physical laws. The measured properties are close to those of bulk sterling silver values—with the noticeable exception of the Young's modulus that is an order of magnitude smaller.

We measured the electrical and mechanical properties of the samples along the printed layers. However, the material fuses after annealing, which, to the best of our knowledge, should yield a fairly isotropic material (see for example the experimental results from SS 316L structures 3D-printed at room temperature via inkjet binder printing and annealed at high temperature [16]). The exploration of the dependence of the physical properties of the printed and annealed parts on the orientation of the layers is outside the scope of this work.

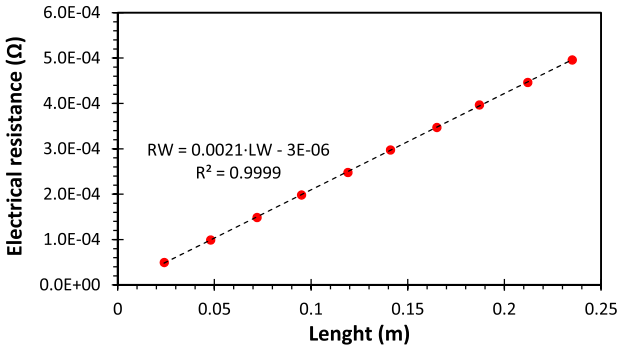

Fig. 10. Electrical resistance versus probe separation for a printed and annealed wire. In the least-squares fitting, RW = electrical resistance, LW = wire length.

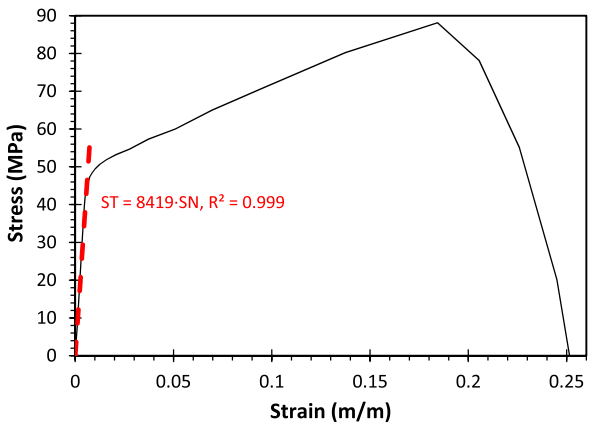

Fig. 11. Stress vs. strain curve of printed and annealed sample. In the least square fitting, ST = uniaxial stress, SN = strain.

A. Electrical Resistivity

Six long and narrow wires were printed and annealed to characterize the electrical resistivity of the material. Each wire, with 10.8 mm^2 nominal cross-sectional area, was placed in a Resistivity Apparatus EM-8812 (Pasco, Roseville, CA, USA) and electrical resistance values for different lengths of the wire were measured with a multimeter Fluke 8846 A (Fluke Corporation, Everett, WA, USA); the resistivity versus length data from of one of the samples are shown in Fig. 10; the other samples yielded similar results. The least-squares fitting of the data shows a linear dependence between the length of the wire and its electrical resistance, in agreement with Ohm's law. The electrical resistivity of the material, ρ, was calculated using the equation

$$R = \frac{\rho}{A_w} X + 2R_c \tag{1}$$

where R is the resistance of the wire, R_c is the contact resistance, A_w is the cross-sectional area of the wire and X is the distance between probes. From the slope of the least-squares fitting, an electrical resistivity of 22.7 $n\Omega \cdot m$ is estimated, which is 19% larger than the literature value for sterling silver (88% IACS, or 19.0 $n\Omega \cdot m$ [28]).

B. Thermal Conductivity

The thermal conductivity of the printed and annealed feedstock was determined using the Wiedemann-Franz law [29] that states that the ratio between the thermal conductivity k and electrical conductivity σ is proportional to the temperature T, i.e.

$$\frac{k}{\sigma} = L_o T \tag{2}$$

where L_o is the Lorentz number, whose value is $2.4 \times 10^{-8} W \cdot \Omega/K^2$ for most metals at 298 K. Based on the results of Section V.A, the electrical conductivity of the printed and annealed material is estimated at $4.4 \times 10^7 S.m^{-1}$ (i.e. the inverse of the estimated electrical resistance); therefore, the thermal conductivity of the printed and annealed material is estimated at 314.7 W/m·K, which is 13% smaller than the reported value for bulk sterling silver in the literature (361 W/m·K [30]).

C. Young's Modulus, Yield Stress, Ultimate Tensile Stress

The Young's modulus, yield stress, and ultimate tensile stress of the printed and annealed material were estimated via uniaxial tensile tests of samples. Six samples were manufactured conforming with American Society for Testing and Materials (ASTM) standard E8/E8M-08. The tensile tests were performed using a materials testing system 5500R (Instron, Norwood, MA, USA) while applying a deformation rate of 10^{-4} mm/s. The stress and strain data were automatically calculated from the raw data (i.e. applied force and deformation) by the software that controls the instrument; the stress-strain curve from one of the samples tested is shown in Fig. 11; the other samples yielded similar results. The material is clearly ductile: the transition from the elastic region to the plastic region is quite sharp, followed by a plateau deformation region with relatively low strain hardening rate. In Fig. 11, the strain gradually increases as the material continues to plastically deform, reaching its maximum value when the strain is equal to 0.18 m/m; the material then weakens until a strain of 0.25 m/m is reached, at which point the material fractures. According the plot, the yield strength is about 48 MPa at 0.008 m/m strain, while the ultimate tensile stress is estimated at 88 MPa at 0.18 m/m strain—both stress values are in agreement with those reported for bulk, undoped, annealed sterling silver (50 MPa ±10 MPa and 90 MPa ± 20 MPa, respectively [31]). From the slope of the linear part of the stress-strain curve, a Young's modulus equal to 8.2 GPa is obtained, which is an order of magnitude smaller than reported bulk values [32]; the sharp difference in the Young's modulus should be further studied. Nonetheless, the data demonstrate that the printed and annealed material is not fragile and can withstand stress levels compatible with bulk values.

A material with a large Young's modulus can be used in applications that require high stiffness, e.g. to keep the deformation below a certain threshold. Consequently, microfluidics made of a high Young's modulus material would be easier to integrate with other structures while keeping tight dimensional tolerances within the system, for example, as part of a deployable system, e.g. an unmanned air vehicle, a nanosatellite, or a handheld device. Any loads, internal or external to the microfluidic, would change little the dimensions of the microfluidic; consequently, its allocated space within the deployable system will change very little. Examples of these microfluidics include miniature hydrogen peroxide monopropellant rockets, heat exchangers, and steam generators for

handheld biological decontamination. In particular, in a heat exchanger the internal pressure of the fluid could be greatly augmented to increase in the same proportion the flow rate, without causing significant deformation of its pipes.

VI. Example: Microreactor for Catalytic Decomposition of Hydrogen Peroxide

The physical properties of the annealed and printed feedstock, in combination with the metrology characterization of printed and annealed structures, suggest that silver clay extrusion is a 3D printing technique suitable to create microfluidics for applications such as heat transfer and chemical processing. In particular, silver is an oxidation catalyst, e.g. utilized in the industry to oxidize ethylene to create ethylene oxide (widely used in applications such as detergents, textiles, pharmaceuticals) and to oxidize methanol to create formaldehyde (widely used in applications such as cars, textiles, adhesives) [33]. Also, silver can act as an electron donor catalyst, e.g. to decompose hydrogen peroxide.

Hydrogen peroxide is a water-soluble oxidant that self-decomposes in the presence of heat or a catalyst. Various materials such as iron chloride [34], silver [35], [36], platinum [37], manganese dioxide [38] and perovskites [39] have been used as catalyst to strike or increase the speed of decomposition of hydrogen peroxide; in particular, silver is an attractive catalyst for hydrogen peroxide decomposition due to its high efficiency [40]. The catalytic decomposition of hydrogen peroxide results in the formation of a two-phase flow of oxygen (gas phase) and water (liquid phase); the reaction liberates enough heat that, under the right conditions, transforms water into steam. The by-products of the catalytic decomposition of hydrogen peroxide could be used for a great variety of PowerMEMS including monopropellant rockets, fuel cells, and ejector pumps [41]–[45].

In this section, we report the design, fabrication and characterization of a proof-of-concept, monolithic microreactor that catalytically decomposes hydrogen peroxide. Unlike reported work, e.g. [45], our microreactor does not require an external source of catalyst since the device is fully made of silver. The device takes 12 min to print, 4 hours to anneal, and costs $25 dollars in printable feedstock. The microreactor operates as predicted by the reduced-order modeling, attaining 87% decomposition efficiency for 5 μL/min flow rate of hydrogen peroxide with 30% w/w initial concentration.

A. Microreactor Design

The proof-of-concept catalytic microreactor is a block of 3D-printed sterling silver with a watertight, 2.5 cm-long, straight, closed microchannel with 600 μm by 600 μm cross-section and a fluidic port at both ends (Fig. 12). The device was manufactured by extruding silver metal clay in 200 μm layers. The fluidic ports are connected to standard metal fittings to feed the hydrogen peroxide and remove the byproducts using Tygon tubes. As hydrogen peroxide flows through the microchannel, the reactant contacts the walls of the microchannel, triggering a catalytic decomposition. For testing, the microfluidic was covered in epoxy to minimize heat losses hence decompose as much as possible the hydrogen peroxide fed to the microfluidic.

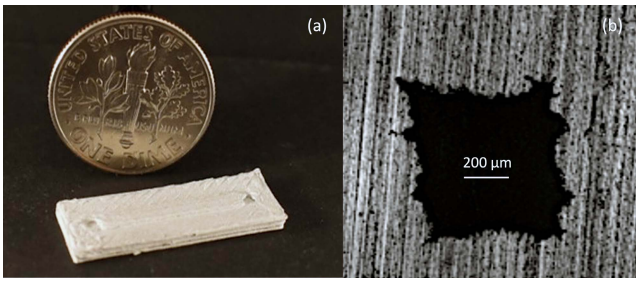

Fig. 12. (a) Extruded monolithic catalytic microreactor with two ports and a watertight, closed microchannel next to a US dime; (b) cross-section of microchannel.

TABLE I
Behavior of State Variables at Each Flow Stage

	Stage 1	Stage 2	Stage 3	Stage 4	Stage 5
Y_P	↓	↓	↓	↓	↓
T	↑	$T_{b,W}$	↑	$T_{b,P}$	↑
f_W	0	↑	1	1	1
f_P	0	0	0	↑	1
Start	$x = 0$	$T = T_{b,W}$	$f_W = 1$	$T = T_{b,P}$	f_P
End	$T = T_{b,W}$	$f_W = 1$	$T = T_{b,P}$	$f_P = 1$	$Y_P = 0$

in Table 1, ↑ means increasing, ↓ means decreasing, $T_{b,W}$ is the boiling point of water, and $T_{b,P}$ is the boiling point of hydrogen peroxide.

B. Microreactor Modeling

A bulk, one-dimensional model was employed to simulate the dynamics of the microreactor because the reactor length is many times (>40) the hydraulic diameter of the microchannel. The flow in the microreactor passes through five stages, as the thermodynamic phases of the species change [46]:

- In stage 1, liquid hydrogen peroxide decomposes into liquid water, oxygen, and heat, which increases the temperature of the species up to the boiling temperature of water;
- In stage 2, water changes phase at constant temperature, becoming steam;
- In stage 3, the liquid hydrogen peroxide decomposes into steam and oxygen, and the heat released further increases the temperature of the species, until the boiling temperature of the hydrogen peroxide at the reactor pressure is reached;
- In stage 4, the hydrogen peroxide changes phase at constant temperature, becoming gaseous.
- Finally, in stage 5 any remnant hydrogen peroxide in gas form decomposes into steam, oxygen, and heat.

Following [36] and [46], a state-space model of these stages was implemented in Mathematica (Wolfram, Champaign, IL, USA) using as state variables the flow temperature T, the hydrogen peroxide mass fraction Y_P, the hydrogen peroxide quality f_P, and the water quality f_W (Table I). Mass and energy conservation were enforced, and species transport was modeled to study the evolution of the state variables versus distance x along the reactor flow length, while accounting for the chemical reaction and the heat loss from the walls of the microfluidic. The chemical decomposition of hydrogen peroxide is given by

$$2H_2O_2 \rightarrow 2H_2O + O_2 + Q \tag{3}$$

where Q is the molar heat release rate; the rate of change of the mass fraction of hydrogen peroxide is given by

$$\frac{dY_P}{dx} = -\frac{M_P R_r A}{\dot{m}} \tag{4}$$

where M_P is the molar mass of peroxide, R_r is the reaction rate, A is the reactor cross-sectional area, and $\dot{m}$ is the total mass flow rate. The equation for conservation of energy is

$$\dot{m}\bar{c}_P \frac{dT}{dx} + \dot{m}Y_P h_{fg,P} \frac{df_P}{dx} + \dot{m}Y_W h_{fg,W} \frac{df_W}{dx} = -\Delta H_R R_r A - \frac{dQ_{loss}}{dx} \tag{5}$$

where $\bar{c}_P$ is the mass-weighted average specific heat of the flow, $h_{fg,P}$ and $h_{fg,W}$ are the enthalpies of vaporization of the hydrogen peroxide and of water, respectively, ΔH_R is the heat of reaction, and Q_{loss} is the rate of heat loss through the reactor walls; $\bar{c}_P$, $h_{fg,P}$, $h_{fg,W}$, and ΔH_R are tabulated in the literature as empirical functions of temperature [47]. The reaction rate R_r is the number of moles of peroxide reacting per unit time and unit reactor volume, given by

$$R_r = \frac{k\rho Y_P}{M_P} \tag{6}$$

where k is the reaction rate constant [46], [48].

The rate loss of heat dQ_{loss}/dx causes the temperature of the flow to decrease, preventing the decomposition of the hydrogen peroxide. The flow loses heat by internal convection to the walls of the microreactor, and then by conduction through the microreactor walls and natural convection from the exposed surface of the device. Therefore, to minimize heat loss, the device was covered with the epoxy Propoxy20 (HCC Holdings, Inc., Cleveland, OH, USA), which has a similar Young's modulus than that estimated in the uniaxial tests (4.6 GPa) and can withstand up to 149 °C.

The steady-state heat transfer between the flow within the microreactor and the ambient was modeled with a thermal resistance network. In the model, the device walls are assumed isothermal because the conduction thermal resistance of the microreactor walls is very small compared to the thermal resistance due to flow convection; therefore, all convection thermal resistances of each m-differential of the microreactor, $R_{conv,m}$, are in parallel, i.e. connect between the flow temperature of the m-differential, T_m, and the wall temperature, T_{wall}. The conduction thermal resistance of the package, R_{pack}, connects between the reactor wall temperature and the ambient temperature T_∞.

The convection resistance of the m-differential, $R_{conv,m}$, is given by

$$R_{conv,m} = \frac{1}{h_{conv} dA_{surf}} \tag{7}$$

where h_{conv} is the convection coefficient (estimated from empirical heat transfer correlations [49]) and dA_{surf} is the differential surface area over which convection takes place, i.e.

$$dA_{surf} = 2dx\,[C_H + C_W] \tag{8}$$

where dx is the length differential along the flow, C_H is the microchannel height and C_D is the microchannel width.

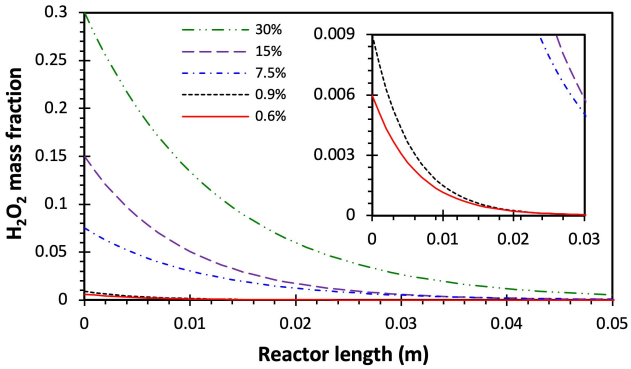

Fig. 13. Hydrogen peroxide mass fraction versus distance along the reactor, with inset close-up of the 0.6% and 0.9% w/w hydrogen peroxide concentration curves for the length of the microreactor.

Therefore, at each m-differential of the microreactor, the heat loss per unit of length from the flow can be written as

$$\frac{dQ_{loss,m}}{dx} = \frac{d}{dx}\left(\frac{T_m - T_{wall}}{R_{conv,m}}\right) = 2h_{conv}\,(T_m - T_{wall})\,[C_H + C_W] \tag{9}$$

The wall temperature is found by iteration while enforcing conservation of energy, i.e.

$$\sum_{m=1}^{n} \frac{T_m - T_{wall}}{R_{conv,m}} = \frac{T_{wall} - T_\infty}{R_{pack}}; \tag{10}$$

R_{pack} is also iterated to find the minimum value at which full peroxide decomposition and water vaporization is attained for a given hydrogen peroxide concentration (1.8% w/w) and flow rate(5 μL/min); the minimum value of the thermal resistance of the package is 27 K/W, which was used in the state-variable model previously described to model Q_{loss}.

Using the tabulated values of the different parameters with the geometry of the microchannel, the mass fractions of the different species were estimated as a function of the reactor length; the result for the mass fraction of hydrogen peroxide is shown in Fig. 13. From this analysis, it was confirmed that the microreactor is able to fully react a flow rate of hydrogen peroxide equal to 5 μL/min with a concentration as high as 1.8% w/w.

C. Microreactor Characterization

To characterize the microreactor design, a syringe pump (NE-1000 New Era Pump Systems, Inc., Farmingdale, NY, USA) was used to supply hydrogen peroxide at a specific flow rate through the microreactor inlet (Fig. 14). Catalytic decomposition of the reactant begins as soon as the hydrogen peroxide interacts with the walls of the microchannel. The liquid by-products that come out of the outlet port of the microreactor are collected in a tank connected to the down-outlet of a T fitting connected to a tube attached to the microreactor outlet port, while the oxygen produced in the reaction escapes through the up-outlet of the T fitting. The liquid phase residues collected in the tank are analyzed with a refractometer Atago PAL-39S, (Atago USA, Inc., Bellevue, WA, USA) to determine the final concentration of hydrogen peroxide after passing through the microreactor. The experimental setup was verified using water to detect leaks before hydrogen peroxide was flown into the microreactor.

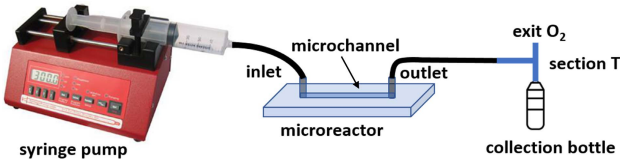

Fig. 14. Experimental setup to characterize catalytic microfluidic that decomposes hydrogen peroxide.

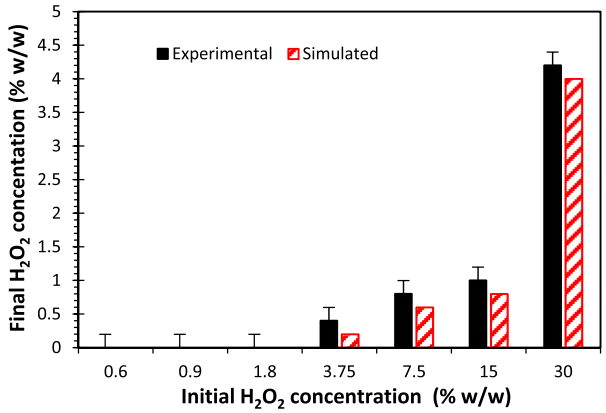

Fig. 15. Summary of effectiveness of hydrogen peroxide decomposition by the catalytic microreactor, i.e. final hydrogen peroxide concentration vs. initial hydrogen peroxide concentration. In all cases, the flow rate is 5 μL/min.

In the experiments, 1 mL of hydrogen peroxide (Hydrogen peroxide solution 30% (w/w) in H_2O, Sigma-Aldrich, St. Louis, MO, USA) at a given concentration (w/w, mixed with deionized water) is loaded to the syringe and allowed to flow at 5 μL/min. During filling-in of the syringe, care was taken so that the air trapped inside the channel was completely removed. It was visually confirmed that the decomposition of hydrogen peroxide forms large amounts of oxygen in the form of bubbles and slugs with small amounts of reacted liquid. The same procedure was carried out at other w/w concentrations of hydrogen peroxide. The concentrations used in the experiments are 0.6%, 0.9%, 1.8%, 3.75%, 7.5%, 15% and 30% (the latter is the concentration of the source of hydrogen peroxide employed in this study).

The microreactor was characterized, decomposing 5 μL/min flow rate of 30% w/w initial hydrogen peroxide concentration with 87% efficiency (Fig. 15). The microreactor was designed for total decomposition of hydrogen peroxide for concentrations below 1.8%; such decomposition was carried out with 100% efficiency. Tests carried out at higher concentrations show that the decomposition of hydrogen peroxide is not complete, where higher initial concentration implies higher final concentration. The experimental results agree with the reduced-order model and theoretical design of the microreactor.

The reported catalytic microreactor is intended as a proof-of-concept demonstration of the feasibility to use silver clay extrusion to create watertight microfluidics; it was not designed with an application in mind. However, it would be straightforward to increase the efficiency of the microreactor for higher initial concentration, specifically by

- Increasing the length of the microreactor. Fig. 13 shows that for a given flow rate and microchannel cross-section, a longer reactor can completely react a larger w/w concentration of hydrogen peroxide. Based on our model, a 10 cm-long, 600 μm by 600 μm microchannel would completely decompose a flow rate of 5 μL/min with up to 30% w/w hydrogen peroxide concentration.
- Reducing the flow rate of hydrogen peroxide per microchannel by flowing the liquid thought several channels in parallel (this increases the surface-to-volume ratio of the liquid for a given total flow rate). Fig. 16 shows the percentage of reaction (i.e. final hydrogen peroxide concentration over initial hydrogen peroxide concentration) versus flow rate of 30% w/w hydrogen peroxide for a microchannel with 600 μm by 600 μm cross-section and 2.5 cm length, evidencing that a smaller flow rate implies a more complete reaction.

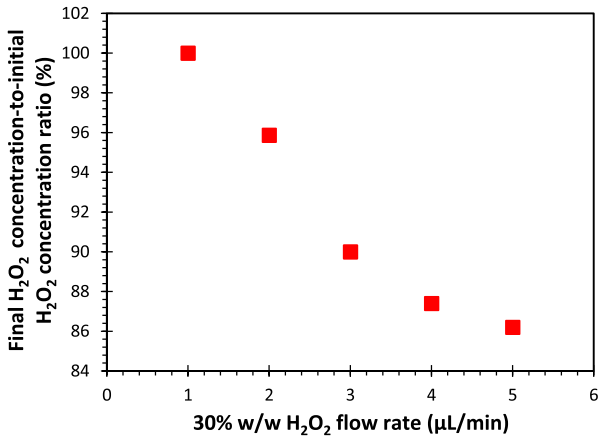

Fig. 16. Ratio between final and initial hydrogen peroxide concentrations versus 30% w/w hydrogen peroxide flow rate for a microchannel with 600 μm by 600 μm cross-section and 2.5 cm length. Full decomposition of the hydrogen peroxide is achieved at 1 μL/min flowrate.

VII. Conclusion

This work explored the use of silver clay extrusion to implement low-cost, monolithic, robust microfluidics. Metrology of positive in-plane, positive out-of-plane, and negative in-plane dimensions of green structures are about 92% CAD values, while in-plane dimensions of positive, annealed structures are about 81% CAD values; out-of-plane dimensions of positive, annealed structures are within about 6% of CAD values, and in-plane negative features part of annealed samples are about 80% CAD values. Watertight closed microchannels as narrow as 200 μm were consistently resolved.

Analysis of the printable feedstock shows that the green material is composed of silver and copper microparticles blended with an organic binder matrix, while the annealed material is sterling silver completely free of binder. Characterization of the electrical resistivity, thermal conductivity, and mechanical properties of the printed and annealed material result in values close of those of bulk sterling silver, except for a significantly smaller Young's modulus for the printed and annealed parts.

Finally, the design, fabrication, and characterization of a proof-of-concept catalytic microreactor that decomposes hydrogen peroxide was reported. The experimental results are in agreement with our modeling, including the complete

decomposition of hydrogen peroxide with initial w/w concentration up to 1.8 % and 5 μL/min flow rate, and 87% decomposition efficiency when the initial hydrogen peroxide w/w concentration is increased to 30%. The reported 3D printing method is compatible with heat transfer and microreactor microfluidic applications, e.g. compact heat exchangers, nanosatellite monopropellant rockets, and handheld steam generators for biological decontamination.

REFERENCES

[1] G. M. Whitesides, "The origins and the future of microfluidics," *Nature*, vol. 442, no. 7101, pp. 368–373, Jul. 2006, doi: 10.1038/nature05058.

[2] A. Manz, N. Graber, and H. M. Widmer, "Miniaturized total chemical analysis systems: A novel concept for chemical sensing," *Sens. Actuators B, Chem.*, vol. 1, nos. 1–6, pp. 244–248, Jan. 1990, doi: 10.1016/0925-4005(90)80209-I.

[3] M. J. Madou, *Fundamentals of Microfabrication: The Science of Miniaturization*, 2nd ed. Boca Raton, FL, USA: CRC Press, 2002.

[4] T. D. Boone, Z. H. Fan, H. H. Hooper, A. J. Ricco, H. Tan, and S. J. Williams, "Peer reviewed: Plastic advances microfluidic devices," *Anal. Chem.*, vol. 74, no. 3, pp. 78 A–86 A, Feb. 2002, doi: 10.1021/ac021943c.

[5] F. Trachsel, C. Hutter, and P. Vonrohr, "Transparent silicon/glass microreactor for high-pressure and high-temperature reactions," *Chem. Eng. J.*, vol. 135, pp. S309–S316, Jan. 2008, doi: 10.1016/j.cej.2007.07.049.

[6] S. Marre, J. Baek, J. Park, M. G. Bawendi, and K. F. Jensen, "High-pressure/high-temperature microreactors for nanostructure synthesis," *J. Assoc. Lab. Automat.*, vol. 14, no. 6, pp. 367–373, Dec. 2009, doi: 10.1016/j.jala.2009.06.005.

[7] L. F. Velásquez-García, T. F. Hill, B. A. Wilhite, K. F. Jensen, A. H. Epstein, and C. Livermore, "A MEMS singlet oxygen generator—Part I: Device fabrication and proof of concept demonstration," *J. Microelectromech. Syst.*, vol. 16, no. 6, pp. 1482–1491, Dec. 2007, doi: 10.1109/JMEMS.2007.902446.

[8] M. F. Shafique, A. Laister, M. Clark, R. E. Miles, and I. D. Robertson, "Fabrication of embedded microfluidic channels in low temperature co-fired ceramic technology using laser machining and progressive lamination," *J. Eur. Ceram. Soc.*, vol. 31, no. 13, pp. 2199–2204, Nov. 2011, doi: 10.1016/j.jeurceramsoc.2011.05.039.

[9] P. Sarma and P. K. Patowari, "Fabrication of metallic micromixers using WEDM and EDM for application in microfluidic devices and circuitries," *Micro Nanosyst.*, vol. 11, pp. 137–147, Nov. 2018, doi: 10.2174/1876402911666181128125409.

[10] X. Ku, Z. Zhang, X. Liu, L. Chen, and G. Li, "Low-cost rapid prototyping of glass microfluidic devices using a micromilling technique," *Microfluidics Nanofluidics*, vol. 22, no. 8, p. 8, Aug. 2018, doi: 10.1007/s10404-018-2104-y.

[11] H. Gong, A. T. Woolley, and G. P. Nordin, "High density 3D printed microfluidic valves, pumps, and multiplexers," *Lab Chip*, vol. 16, no. 13, pp. 2450–2458, 2016, doi: 10.1039/C6LC00565A.

[12] N. Bhattacharjee, A. Urrios, S. Kang, and A. Folch, "The upcoming 3D-printing revolution in microfluidics," *Lab Chip*, vol. 16, no. 10, pp. 1720–1742, 2016, doi: 10.1039/C6LC00163G.

[13] A. L. Beckwith, J. T. Borenstein, and L. F. Velásquez-García, "Monolithic, 3D-printed microfluidic platform for recapitulation of dynamic tumor microenvironments," *J. Microelectromech. Syst.*, vol. 27, no. 6, pp. 1009–1022, Dec. 2018, doi: 10.1109/JMEMS.2018.2869327.

[14] E. García-López, D. Olvera-Trejo, and L. F. Velásquez-García, "3D printed multiplexed electrospinning sources for large-scale production of aligned nanofiber mats with small diameter spread," *Nanotechnology*, vol. 28, no. 42, Oct. 2017, Art. no. 425302, doi: 10.1088/1361-6528/aa86cc.

[15] L. F. Velásquez-García, "SLA 3-D printed arrays of miniaturized, internally fed, polymer electrospray emitters," *J. Microelectromech. Syst.*, vol. 24, no. 6, pp. 2117–2127, Dec. 2015, doi: 10.1109/JMEMS.2015.2475696.

[16] Z. Sun, G. Vladimirov, E. Nikolaev, and L. F. Velasquez-Garcia, "Exploration of metal 3-D printing technologies for the microfabrication of freeform, finely featured, mesoscaled structures," *J. Microelectromech. Syst.*, vol. 27, no. 6, pp. 1171–1185, Dec. 2018, doi: 10.1109/JMEMS.2018.2875158.

[17] R. Frykholm, Y. Takeda, B.-G. Andersson, and R. Carlström, "Solid state sintered 3-D printing component by using inkjet (Binder) method," *J. Jpn. Soc. Powder Powder Metall.*, vol. 63, no. 7, pp. 421–426, 2016, doi: 10.2497/jjspm.63.421.

[18] L. Yang, H. Gong, S. Dilip, and B. Stucker, "An investigation of thin feature generation in direct metal laser sintering systems," in *Proc. 26th Annu. Int. Solid Freeform Fabr. Symp.*, 2014, pp. 714–731.

[19] M. Vaezi, H. Seitz, and S. Yang, "A review on 3D micro-additive manufacturing technologies," *Int. J. Adv. Manuf. Technol.*, vol. 67, nos. 5–8, pp. 1721–1754, Jul. 2013, doi: 10.1007/s00170-012-4605-2.

[20] D. Pranzo, P. Larizza, D. Filippini, and G. Percoco, "Extrusion-based 3D printing of microfluidic devices for chemical and biomedical applications: A topical review," *Micromachines*, vol. 9, no. 8, p. 374, Jul. 2018, doi: 10.3390/mi9080374.

[21] K. Hoshino, M. Morikawa, T. Kohno, K. Ueda, and M. Miyakawa, "Moldable mixture for use in the manufacturing of precious metal articles," U.S. Patent 5 328 775, Jul. 12, 1994.

[22] Z. Sun and L. F. Velásquez-García, "Monolithic FFF-printed, biocompatible, biodegradable, dielectric-conductive microsystems," *J. Microelectromech. Syst.*, vol. 26, no. 6, pp. 1356–1370, Dec. 2017, doi: 10.1109/JMEMS.2017.2746627.

[23] D. T. Hartkop, *Build Your Own Mini Metal Maker: 3D Print With Metal Clay, Ceramic, Chocolate, Stem Cells, or Whatever!* Scotts Valley, CA, USA: CreateSpace Independent Publishing Platform, 2016.

[24] E. R. Jette and F. Foote, "Precision determination of lattice constants," *J. Chem. Phys.*, vol. 3, no. 10, pp. 605–616, Oct. 1935, doi: 10.1063/1.1749562.

[25] B. D. Cullity, *Elements of X Ray Diffraction*. Reading, MA, USA: Addison-Wesley, 1956.

[26] R. Wei *et al.*, "Effect of plasticizer dibutyl phthalate on the thermal decomposition of nitrocellulose," *J. Thermal Anal. Calorimetry*, vol. 134, no. 2, pp. 953–969, Nov. 2018, doi: 10.1007/s10973-018-7521-3.

[27] M. K. Trivedi, A. Branton, D. Trivedi, G. Nayak, R. K. Mishra, and S. Jana, "Characterization of physicochemical and thermal properties of biofield treated ethyl cellulose and methyl cellulose," *Int. J. Biomed. Mater. Res.*, vol. 3, no. 6, pp. 83–91, 2015, doi: 10.11648/j.ijbmr.20150306.12.

[28] R. A. Matula, "Electrical resistivity of copper, gold, palladium, and silver," *J. Phys. Chem. Reference Data*, vol. 8, no. 4, pp. 1147–1298, Oct. 1979, doi: 10.1063/1.555614.

[29] R. Franz and G. Wiedemann, "Ueber die Wärme-Leitungsfähigkeit der metalle," *Annalen der Physik und Chem.*, vol. 165, no. 8, pp. 497–531, 1853, doi: 10.1002/andp.18531650802.

[30] S. Vandana, *Alternative Energy*. New Delhi, India: APH Publishing Corporation, 2002.

[31] S. Sakultanchareonchai, T. Chairuangsri, and E. Nidsaratanaporn, "Combined effects of boron, sodium and strontium on grain refinement of sterling silver grade 950," *Chiang Mai J. Sci.*, vol. 38, no. 3, pp. 370–379, 2011.

[32] W. Köster and W. Rauscher, "Relations between the modulus of elasticity of binary alloys and their structure," Nat. Aeronaut. Space Admin., Washington, DC, USA, Tech. Rep. NACA-TM-1321, 1951.

[33] G. C. Bond, "Periodic variations in the catalytic properties of metals," *Platinum Met. Rev.*, vol. 12, no. 3, pp. 100–105, 1968.

[34] J. De Laat and H. Gallard, "Catalytic decomposition of hydrogen peroxide by Fe(III) in homogeneous aqueous solution: Mechanism and kinetic modeling," *Environ. Sci. Technol.*, vol. 33, no. 16, pp. 2726–2732, Aug. 1999, doi: 10.1021/es981171v.

[35] H. J. Baumgartner, G. C. Hood, J. M. Monger, R. M. Roberts, and C. E. Sanborn, "Decomposition of concentrated hydrogen peroxide on silver I. Low temperature reaction and kinetics," *J. Catal.*, vol. 2, no. 5, pp. 405–414, 1963, doi: 10.1016/0021-9517(63)90105-2.

[36] D. Plumlee, J. Steciak, and A. Moll, "Development and simulation of an embedded hydrogen peroxide catalyst chamber in low-temperature co-fired ceramics," *Int. J. Appl. Ceram. Technol.*, vol. 4, no. 5, pp. 406–414, Oct. 2007, doi: 10.1111/j.1744-7402.2007.02161.x.

[37] D. A. MacInnes, "The mechanism of the catalysis of the decomposition of hydrogen peroxide by colloidal platinum," *J. Amer. Chem. Soc.*, vol. 36, p. 878, 1914, doi: 10.1021/ja02182a011.

[38] K. A. Omar, "Catalytic decomposition of hydrogen peroxide on manganese dioxide nanoparticles at different pH values," *Int. J. Res. Eng. Technol.*, vol. 2, no. 5, pp. 241–248, 2014.

[39] M. Soleymani, A. Moheb, and D. Babakhani, "Hydrogen peroxide decomposition over nanosized $La_{1-X}Ca_XMnO_3$ ($0 \leq X \leq 0.6$) perovskite oxides," *Chem. Eng. Technol.*, vol. 34, no. 1, pp. 49–55, Jan. 2011, doi: 10.1002/ceat.201000293.

[40] S.-L. Lee and C.-W. Lee, "Performance characteristics of silver catalyst bed for hydrogen peroxide," *Aerosp. Sci. Technol.*, vol. 13, no. 1, pp. 12–17, Jan. 2009, doi: 10.1016/j.ast.2008.02.007.

[41] J. Xu, Y. Feng, and J. Cen, "Transient flow patterns and bubble slug lengths in parallel microchannels with oxygen gas bubbles produced by catalytic chemical reactions," *Int. J. Heat Mass Transf.*, vol. 50, nos. 5–6, pp. 857–871, Mar. 2007, doi: 10.1016/j.ijheatmasstransfer.2006.08.017.

[42] L. Chiappetta, L. Spadaccini, H. Huang, W. Watkins, and A. Crocker, "Modeling a hydrogen peroxide gas generator for rockets," in *Proc. 36th AIAA/ASME/SAE/ASEE Joint Propuls. Conf. Exhibit*, Las Vegas, NV, USA, Jul. 2000, doi: 10.2514/6.2000-3223.

[43] M. Xiao, L. Wang, F. Ji, and F. Shi, "Converting chemical energy to electricity through a three-jaw mini-generator driven by the decomposition of hydrogen peroxide," *ACS Appl. Mater. Interfaces*, vol. 8, no. 18, pp. 11403–11411, May 2016, doi: 10.1021/acsami.6b00550.

[44] O. Hasvold and K. H. Johansen, "The alkaline aluminium hydrogen peroxide semi-fuel cell for the HUGIN 3000 autonomous underwater vehicle," in *Proc. Workshop Auton. Underwater Vehicles*, San Antonio, TX, USA, Jun. 2002, pp. 89–94, doi: 10.1109/AUV.2002.1177209.

[45] F. Eid, L. F. Velásquez-García, and C. Livermore, "Design, fabrication and demonstration of a MEMS steam generator for ejector pump applications," *J. Micromech. Microeng.*, vol. 20, no. 10, Oct. 2010, Art. no. 104007, doi: 10.1088/0960-1317/20/10/104007.

[46] X. Zhou and D. Hitt, "One-dimensional modeling of catalyzed H_2O_2 decomposition in microchannel flows," in *Proc. 33rd AIAA Fluid Dyn. Conf. Exhibit*, Orlando, FL, USA, Jun. 2003, doi: 10.2514/6.2003-3584.

[47] C. L. Yaws, *Chemical Properties Handbook*. New York, NY, USA: McGraw-Hill, 1999.

[48] R. J. Orr and H. L. Williams, "Kinetics of the reactions between iron(II) and hydroperoxides based upon cumene and cyclohexane," *J. Phys. Chem.*, vol. 57, no. 9, pp. 925–931, Sep. 1953, doi: 10.1021/j150510a016.

[49] A. F. Mills, *Heat Transfer*. Upper Saddle River, NJ, USA: Prentice-Hall, 1999.

Emmanuel Segura-Cárdenas received the B.S. degree in physical engineering, and the M.S. and Ph.D. degrees in applied science from the Universidad Autonoma de San Luis Potosi, San Luis Potosi, Mexico, in 2007, 2009, and 2014, respectively. In 2014, after completing his studies, he held a post-doctoral position at the Nanomaterials Group, Drexel University, Philadelphia, PA, USA. Since 2016, he has been an Adjunct Researcher with the Tecnologico de Monterrey, Monterrey, Mexico, and he carried out a research stay at the Massachusetts Institute of Technology, Cambridge, MA, USA, in 2018. His research focuses on the additive manufacturing of metal and polymeric materials, and the synthesis and characterization of nanomaterials based on carbon for applications in electronic devices.

Luis Fernando Velásquez-García (Senior Member, IEEE) received the degrees *(magna cum laude)* (Valedictorian of the School of Engineering) in mechanical engineering and civil engineering from the Universidad de Los Andes, Bogotá, Colombia, in 1998 and 1999, respectively, and the M.S. and Ph.D. degrees from the Massachusetts Institute of Technology (MIT), Cambridge, MA, USA, in 2001 and 2004, respectively.

In 2004, after completing his studies, he became a Post-Doctoral Associate with Microsystems Technology Laboratories (MTL), MIT, where he was appointed as a Research Scientist in 2005. Since 2009, he has been a Principal Scientist and a Core Member with MTL. He is an expert in micro and nanofabrication technologies. He leads the Micro- and Nano-Enabled Multiplexed Scaled-Down Systems Group, MIT, which conducts fundamental and applied research on miniaturized devices and systems that exploit high-electric field phenomena such as electrospray, gas ionization, field emission, X-rays, and plasmas for space, energy, healthcare, manufacturing, and analytical applications. His work currently focuses on additively manufactured micro and nanosystems. He has authored more than 51 journal and 80 conference proceedings publications, and he holds 12 patents on MEMS/NEMS technologies.

Dr. Velásquez-García is a Full Member of Sigma Xi and a Senior Member of the American Institute of Aeronautics and Astronautics (AIAA). He served as the Co-Chair of the 15th International Conference on Micro and Nanotechnology for Power Generation and Energy Conversion Applications (PowerMEMS 2015). His group's work has received multiple recognitions, including best-paper awards in conferences such as PowerMEMS and Transducers, and best-paper highlights at journals such as the IEEE JOURNAL OF MICROELECTROMECHANICAL SYSTEMS, the *IOP Journal of Physics D: Applied Physics*, the *IOP Journal of Micromechanics and Microengineering*, and *IOP Nanotechnology*.